

# Experimental Demonstration of Single Pulse Imaging (SPI)

David G. Felton, Christian C. Jones, Daniel B. Herr, Lumumba A. Harnett, Shannon D. Blunt,  
Christopher T. Allen

Radar Systems Lab (RSL), University of Kansas (KU), Lawrence, KS

**Abstract**—The single pulse imaging (SPI) algorithm was developed as a means to generalize adaptive pulse compression (APC) by incorporating fast-time Doppler, thereby enhancing separability of scatterers in both range and Doppler. Here, we modify this model-based method by introducing dynamic beamspoiling to provide additional robustness. Open-air experimental results for this robust instantiation of SPI are then shown using an ultrasonic testbed at a center frequency of 47.5 kHz, which is analogous to an RF center frequency of 41.25 GHz. The low propagation velocity and associated wavelength of sound permits meaningful emulation of the high speeds that introduce fast-time Doppler effects for RF operation.

**Index Terms**—Doppler processing, radar imaging, adaptive processing

## I. INTRODUCTION

Legacy radar systems typically gather range and Doppler information via illumination with a repeated waveform such as the linear frequency modulated (LFM) chirp. The repeated illumination and low mover velocities (relative to the speed of light) yield a decoupling of range and Doppler, thereby enabling separation of fast-time (range) and slow-time (Doppler). Range estimation is then performed via pulse compression via a matched/mismatched filter and Doppler estimation is realized by Fourier transform of the phase progression across slow-time. However, higher center frequencies and/or higher radial mover velocities can invalidate the decoupled “stop-and-hop” assumption [1]. Consequently, ambiguities or losses are incurred depending on the type of waveform employed.

For applications where range/Doppler coupling occurs there are two schools of thought. The first, and more traditional, uses a Doppler-tolerant waveform like LFM [2], where tolerance arises because the waveform’s ambiguity function possesses an intrinsic coupling between range and fast-time Doppler, as evidenced by the prominent “delay-Doppler ridge”. While this ridge ensures little loss is incurred when a given scatterer has significant Doppler, it also introduces a delay ambiguity, which can create confusion when multiple high-speed scatterers are present in close proximity.

Alternatively, waveforms having a thumbtack ambiguity function are Doppler *selective* (or *intolerant* depending on one’s perspective). As a result, a Doppler filter bank with sufficient granularity is necessary to cover the expected span of velocities that may be encountered with an acceptable degree

of mismatch loss. However, this increased receive complexity does come with the benefit of avoiding the delay/Doppler ambiguity encountered by LFM and other Doppler-tolerant waveforms.

While the Doppler selectivity of thumbtack waveforms provides mainlobe separability for scatterers at different velocities, there still remains the issue of sidelobes, whereby a large scatterer can mask a nearby smaller scatterer. The reiterative minimum-mean-square-error (RMMSE) [3] formulation first developed to perform adaptive pulse compression (APC) takes an adaptive nulling approach in which a unique filter is created for each individual range cell, thereby suppressing sidelobes induced by other nearby scatterers. By subsequently incorporating appropriate robustness measures, this formulation has since been experimentally demonstrated in the APC context [4] and has likewise been used for adaptive beamforming [5, 6], brain imaging [7], active sonar [8], weather radar [9], synthetic aperture radar (SAR) [10], Doppler estimation [11, 12], and adaptive spectrogram estimation [13].

The single pulse imaging (SPI) [14, 15] algorithm was first proposed in 2006 as a fast-time Doppler extension of the RMMSE-based multistatic adaptive pulse compression (MAPC) [16] algorithm, where the various Doppler-shifted versions of the transmitted signal are treated (by SPI) as distinct waveforms illuminating distinct scattering such as one encounters in a multistatic setting. Consequently, the adaptive nulling procedure to suppress interfering sidelobes is generalized to include both range and fast-time Doppler, thereby realizing enhanced sensitivity. The same idea was later used for the iterative adaptive approach (IAA) method derived in a least-squares context [17], with [18] noting that RMMSE (prior to the robustness measures noted above) and IAA are actually equivalent.

The previous work on SPI [14, 15] examined simulated scenarios. Here we apply this approach to experimental measurements obtained from an ultrasonic testbed. As part of this examination, it has been observed that further robustness from unavoidable model mismatch is required, which is now incorporated into a modified version of SPI.

## II. RECEIVE SIGNAL MODEL

Consider the continuous waveform  $s(t)$ , for which a delay and Doppler shifted version can be expressed as

$$\tilde{s}(t) = s\left(t - \frac{2v}{c}t\right) \quad (1)$$

for  $c$  the speed of light and  $v$  the Doppler-inducing radial velocity (positive/negative if approaching/receding). Now discretize the transmitted waveform as  $\mathbf{s} \in \mathbb{C}^{N \times 1}$ , noting that the pulsed nature means the signal cannot be bandlimited, and thus some degree of aliasing is unavoidable. Consequently, “over-sampling” with respect to a measure of the passband bandwidth (e.g. 3-dB) is necessary to achieve sufficiently low aliasing depending on the waveform’s spectral roll-off. Neglecting relativistic effects, a fast-time Doppler-shifted replica in discretized form can then be represented as

$$\tilde{\mathbf{s}}_k = \mathbf{s} \odot \mathbf{p}_k \quad (2)$$

where  $\odot$  is the Hadamard product and the  $N \times 1$  phase progression vector

$$\mathbf{p}_k = [1 \quad e^{j\theta_k} \quad \dots \quad e^{j(N-1)\theta_k}]^T \quad (3)$$

represents the fast-time frequency shift (with each  $\theta_k$  proportional to a discretized value of radial velocity  $v$ ). Here

$$\theta_k = -\pi + 2\pi \frac{k-1}{K-1}, \quad k = 1, \dots, K \quad (4)$$

spans the  $2\pi$  phase space with sufficient granularity, though a smaller portion may be feasible depending on the particular application and system parameters.

We can effectively treat the received signal as a superposition of distinct scattering induced by distinct Doppler-shifted waveforms. The discretized received signal vector  $\mathbf{y}(\ell) = [y(\ell) \quad \dots \quad y(\ell + N - 1)]^T$  corresponding to the  $\ell^{\text{th}}$  range delay index is then

$$\mathbf{y}(\ell) = \sum_{k=1}^K \mathbf{S}_k \mathbf{x}_k(\ell) + \mathbf{v}(\ell) \quad (5)$$

where  $\mathbf{v}(\ell)$  is additive noise of an arbitrary distribution. The  $n^{\text{th}}$  column of matrix  $\mathbf{S}_k \in \mathbb{C}^{(N \times 2N-1)}$  contains  $\tilde{\mathbf{s}}_k$  shifted by  $n - N$  samples and zero filled so that

$$\mathbf{S}_k = [\tilde{\mathbf{s}}_{k,1-N} \quad \tilde{\mathbf{s}}_{k,2-N} \dots \tilde{\mathbf{s}}_{k,N-1}] \quad (6)$$

(i.e.,  $\tilde{\mathbf{s}}_{k,-2} = [s_k(2) \quad \dots \quad s_k(N-1) \quad 0 \quad 0]^T$ ). The range profile vector

$$\mathbf{x}_k(\ell) = [x_k(\ell - N + 1) \quad \dots \quad x_k(\ell + N - 1)]^T$$

contains the  $2N-1$  complex contiguous scattering coefficients surrounding the  $\ell^{\text{th}}$  range cell and corresponding to the  $k^{\text{th}}$  discretized Doppler shift.

### III. REVIEW OF SINGLE PULSE IMAGING (SPI)

Let  $\mathbf{w}_k(\ell)$  denote the pulse compression filter that estimates the scattering at the  $\ell^{\text{th}}$  delay and  $k^{\text{th}}$  Doppler shift via

$$\hat{x}_k(\ell) = \mathbf{w}_k^H(\ell) \mathbf{y}(\ell). \quad (7)$$

For the standard non-adaptive approach, it is convenient to normalize this Doppler-tuned matched filter as

$$\mathbf{w}_k(\ell) = \frac{\tilde{\mathbf{s}}_k}{\|\tilde{\mathbf{s}}_k\|^2}, \quad (8)$$

the collection of which across the Doppler indices  $k$  comprise a filter bank. While the matched filter maximizes signal-to-noise ratio (SNR), it does not address the estimation interference induced by the range/Doppler sidelobes of other scatterers.

Like its RMMSE predecessors, the SPI algorithm [14, 15] poses the MMSE cost function for the  $\ell^{\text{th}}$  range cell of the  $k^{\text{th}}$  range profile as

$$J(\ell, \theta_k) = \mathbb{E} \{ |x_k(\ell) - \mathbf{w}_k^H(\ell) \mathbf{y}(\ell)|^2 \}, \quad (9)$$

where  $\mathbb{E} \{ \bullet \}$  is the expectation operator and  $x_k(\ell)$  is the scattering ground truth we wish to estimate. Using the matched filter response from (8) to obtain the initial scattering estimates  $\hat{x}_{k,0}(\ell)$  for  $k$  and  $\ell$ , the underlying RMMSE framework adaptively provides an updated version of the filter via

$$\mathbf{w}_{k,i}(\ell) = \hat{\rho}_{k,i}(\ell) (\mathbf{R}_{s,i} + \mathbf{R}_{z,i} + \mathbf{R}_v)^{-1} \tilde{\mathbf{s}}_k, \quad (10)$$

where  $i$  denotes iteration index and  $\hat{\rho}_{k,i}(\ell) = |\hat{x}_{k,i}(\ell)|^2$  is the current power estimate of the given range-Doppler cell. The structured signal covariance matrix

$$\mathbf{R}_{s,i} = \sum_{k=1}^K \mathbf{S}_k \mathbf{P}_{k,i}(\ell) \mathbf{S}_k^H \quad (11)$$

likewise contains these current power estimates in the form of the source covariance matrix

$$\mathbf{P}_{k,i}(\ell) = [\hat{\mathbf{x}}_{k,i}(\ell) \hat{\mathbf{x}}_{k,i}^H(\ell)] \odot \mathbf{I}_{2N-1} \quad (12)$$

in which  $\mathbf{I}$  is a  $2N-1 \times 2N-1$  identity matrix and scatterers have been assumed to be uncorrelated. The term

$$\mathbf{R}_v = \mathbb{E} \{ \mathbf{v}(\ell) \mathbf{v}^H(\ell) \} = \sigma_v^2 \mathbf{I}_N \quad (13)$$

is the noise correlation matrix, which for simplicity we assume to be white Gaussian with noise power  $\sigma_v^2$ , though doing so is not a requirement. The remaining term

$$\mathbf{R}_{z,i} = \sigma_z^2 [\mathbf{R}_{s,i} \odot \mathbf{I}_N] \quad (14)$$

arises from the realization [5] that model mismatch is unavoidable and therefore provides an additional diagonal weighting based on model uncertainty variance  $\sigma_z^2$ . Determination of this value is application and system dependent. Computational complexity of the matrix inversion in (10) clearly increases with waveform dimensionality and Doppler granularity, though efficient implementations exists [19] that seek to alleviate this burden. And while a coarse partitioning in Doppler can also ease computational cost, it does so at the expense of signal degradation due to straddling effects. Setting  $2N < K < 10N$  has been found to work well, while excessively large  $K$  yields little practical benefit and could also induce numerical instability.

### IV. FURTHER ROBUSTNESS BY DYNAMIC BEAMSPILING

While the inclusions of (14) does provide some robustness against model mismatch, the unconstrained form of (9) still has the tendency to over-suppress small signals as it attempts to fit the measured data to point scatterers. In reality, physical

scattering is a continuum that does not adhere to a point-like model, meaning that range and Doppler straddling [20] is always present. In a move toward alleviating such effects, [21] proposed the incorporation of a unity gain constraint akin to the minimum variance distortionless response (MVDR) beamformer [22], which serves to temper the degree of super-resolution and thereby reduces over-suppression in the RMMSE context. This attribute was later supplemented [4] with a “beamspoil” aspect involving the removal of components in the source correlation matrix (11) that correspond to range cells immediately surrounding a given scatterer, again with the intent of relaxing super-resolution. An alternative beamspoil approach was recently explored in [23] by merging adjacent RMMSE filters. Here a notion similar to [23] is employed at the covariance matrix level.

Consider a localized beamspoil matrix for the  $\ell^{th}$  range cell and  $k^{th}$  Doppler bin that encompasses range-Doppler bins extending  $\pm A$  in range and  $\pm B$  in Doppler, represented as

$$\bar{\mathbf{R}}_{b,i}(\ell, k) = \sum_{k'=k-B}^{k+B} \bar{\mathbf{S}}_{k'} \bar{\mathbf{P}}_{k',i}(\ell) \bar{\mathbf{S}}_{k'}^H. \quad (15)$$

Here  $\bar{\mathbf{S}}_{k'} \in \mathbb{C}^{N \times (2A+1)}$  is the center  $2A+1$  columns of  $\mathbf{S}_{k'}$  from (11) and likewise  $\bar{\mathbf{P}}_{k',i}(\ell) \in \mathbb{R}^{(2A+1) \times (2A+1)}$  is the diagonal matrix of the centermost  $2A+1$  elements in  $\mathbf{P}_{k',i}(\ell)$  from (12). This localized source correlation matrix can be incorporated into the RMMSE filter (10) to provide beamspoil as

$$\bar{\mathbf{w}}_{k,i}(\ell) = (\mathbf{R}_{s,i} + \mathbf{R}_{z,i} + \mathbf{R}_v)^{-1} \bar{\mathbf{R}}_{b,i}(\ell, k) \frac{\tilde{\mathbf{s}}_k}{\|\tilde{\mathbf{s}}_k\|^2}. \quad (16)$$

We observe that, if  $A$  and  $B$  are set equal to zero (the case of no beamspoil) then (16) simplifies to (10) via

$$\begin{aligned} \bar{\mathbf{w}}_{k,i}(\ell) &= (\mathbf{R}_{s,i} + \mathbf{R}_{z,i} + \mathbf{R}_v)^{-1} \tilde{\mathbf{s}}_k \hat{\rho}_{k,i}(\ell) \tilde{\mathbf{s}}_k^H \frac{\tilde{\mathbf{s}}_k}{\|\tilde{\mathbf{s}}_k\|^2} \\ &= \hat{\rho}_{k,i}(\ell) (\mathbf{R}_{s,i} + \mathbf{R}_{z,i} + \mathbf{R}_v)^{-1} \tilde{\mathbf{s}}_k \\ &= \mathbf{w}_{k,i}(\ell). \end{aligned} \quad (17)$$

The beamspoil matrix is effectively undoing the super-resolution (i.e. decorrelating) effect imposed by the inverted matrix so that the estimated response does not collapse to non-physical point scatterers.

## V. EXPERIMENTAL SETUP

To experimentally demonstrate the efficacy of the SPI algorithm, an open-air test was performed using a low-cost ultrasonic testbed. While the speed of sound is significantly slower than the speed of light, the scattering phenomenology is still basically the same (lack of polarization notwithstanding). Moreover, ultrasonic experimentation can be performed at a fraction of the cost of RF and within a much smaller physical footprint. Indeed, this “open-air” test was actually conducted indoors because at such a short wavelength (here  $< 1$  cm) and low transmit power ( $\sim 1$  mW) an indoors vs. outdoors setting really makes no difference. Ultrasonic wavelengths can also

be readily matched to their electromagnetic counterpart to enable experimentation without concern over already congested spectral resources.

A pulsed pseudo-random optimized frequency modulated (PRO-FM) [24] waveform was generated with a center frequency of  $f_c = 47.5$  kHz, a 3-dB bandwidth of  $B = 10$  kHz, and pulse width of  $T = 15$  ms, which provides a nominal range resolution of 1.7 cm and a time-bandwidth product of  $TB = 150$ . This center frequency corresponds to a wavelength of  $\sim 7.2$  mm, which at RF would be associated with an effective center frequency of 41.5 GHz.

An initial open-air “loopback” measurement was performed in which the direct path of the transmitter was used to estimate distortion from the transducer, and fast-time Doppler shifted matched filters were generated using this transmitter-distorted version. Clearly this method of matched filter generation is still imperfect since it inherently assumes the receiver imparts no further distortion and that the Doppler-tuned matched filter bank exactly matches reality, though the incorporation of the model mismatch term in (10) and beamspoil in (16) is sufficient to facilitate adaptive estimation enhancement.

To produce a scene containing a variety of “high-speed” Doppler signatures, a plastic tricycle (see Fig. 1) was attached to a rope and pulled backwards from the receiver. In this way the dynamic motion of the body, wheels, and pedals all produce unique range-Doppler features (exploiting the low speed of sound and short wavelength). The tricycle had a total length of 58.4 cm, with a 25.4 cm front wheel diameter, 14 cm diameter of the back wheels, and pedal radius of 7.6 cm. Sound absorbing material was placed below the tricycle to reduce acoustic noise from the wheels hitting the floor.

The transmit transducer was driven by a Keysight function generator that produced a 10 Vpp replica of the PRO-FM waveform to illuminate the scene. A pulse repetition interval of 31.25 ms captured multiple “looks” of the range-Doppler characteristics as the scene progressed (i.e. as the tricycle moved). The receiver was a wideband ultrasonic transducer (Fig. 2) connected to a real-time spectrum analyzer (RSA) with a sample rate of 100 kHz. While efforts were made to minimize in-band acoustic noise, the function generator and RSA both produced low power spurious noise that was not sufficiently stationary to completely mitigate.

## VI. EXPERIMENTAL RESULTS

Two data collections were made to verify the efficacy of beamspoil SPI. The first consisted of a “quiet scene” in which the tricycle was absent, thereby serving as a baseline measurement of the stationary components in the room, and which was also used for background subtraction. The second collection involved the moving tricycle as described above. This latter dataset was processed with the standard matched filter bank and beamspoil SPI, both without and with background subtraction.

Fig. 3 shows the range-Doppler response when applying a standard matched filter bank via (8). A scattering structure is faintly seen around 0.2 m that is moving at a velocity of +0.5



Fig. 1: “High-speed” tricycle tied to a rope that was pulled to emulate a scene with complex motion

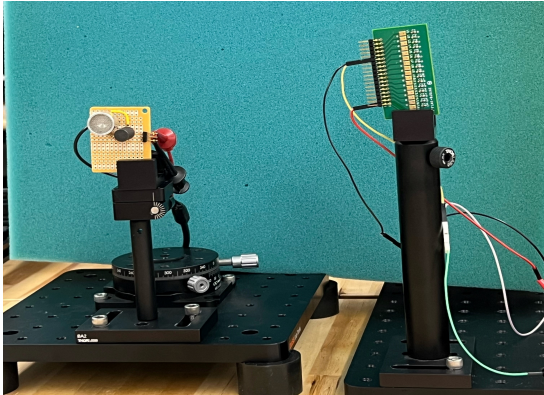


Fig. 2: Transmit transducer (left) and receiver (right) secured to optical breadboard

m/s, though the high sidelobe floor makes the shape and extent of the scattering source nearly indistinguishable from the background. Although simple to implement, the matched filter bank visually provides little meaningful information about the scene aside from the general location and velocity of some scattering “blob”.

Next, seven iterations of beamspoiled SPI were performed on the same data using range beamspoiling of  $A=4$ , Doppler beamspoiling of  $B=3$ , model uncertainty variance of  $\sigma_z^2 = 0.05$ , and noise covariance estimated from the receiver noise. Fig. 4 shows that the high range-Doppler sidelobes have now been significantly reduced and the tricycle scattering centers are clearly visible. While the SPI estimate does appear to match the theoretically expected structure [25], the remaining background scattering does limit determination of whether the estimation floor of noise / model mismatch error is being reached.

We subsequently performed a simple form of background cancellation by subtracting the quiescent response from the “moving” data collection. Fig. 5 shows that performing matched filter processing on the ensuing background-cancelled data does alleviate a notable amount of the sidelobe response caused by background scattering, thereby allowing the moving tricycle to be more visible.

Beamspoiled SPI was then applied to this background-

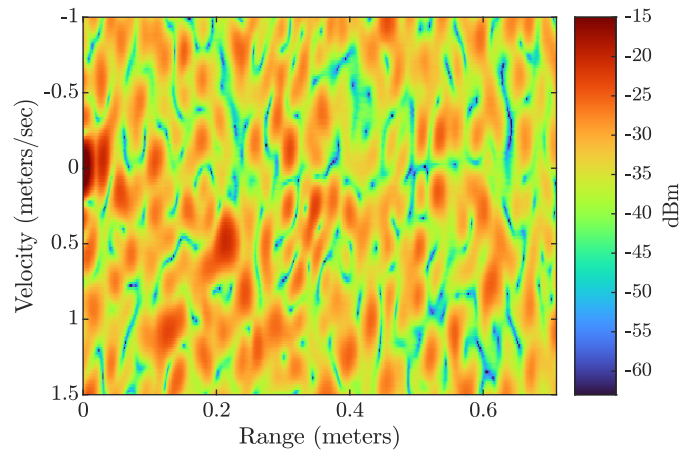


Fig. 3: Range-Doppler image for matched filter processing via (8)

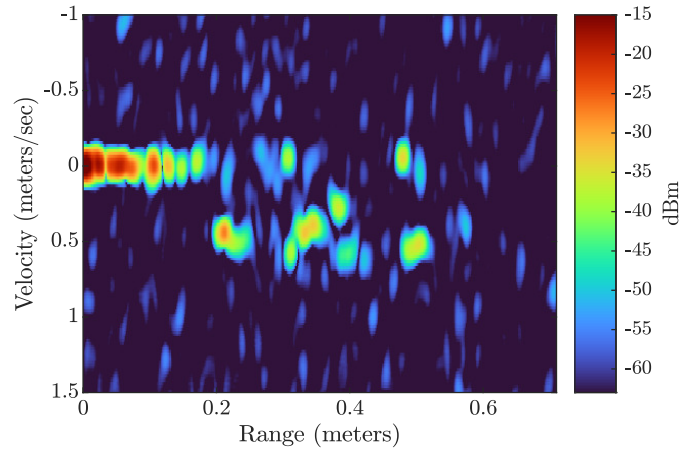


Fig. 4: Range-Doppler image after seven iteration of beamspoiled SPI via (16) with  $A=4$  and  $B=3$

cancelled data using the same parameters as before. Fig. 6 now reveals much greater visibility of individual scattering centers, with the general shape and extent of the tricycle readily apparent.

To examine the signature and features of the tricycle as time progresses, the subsequent two pulses processed with

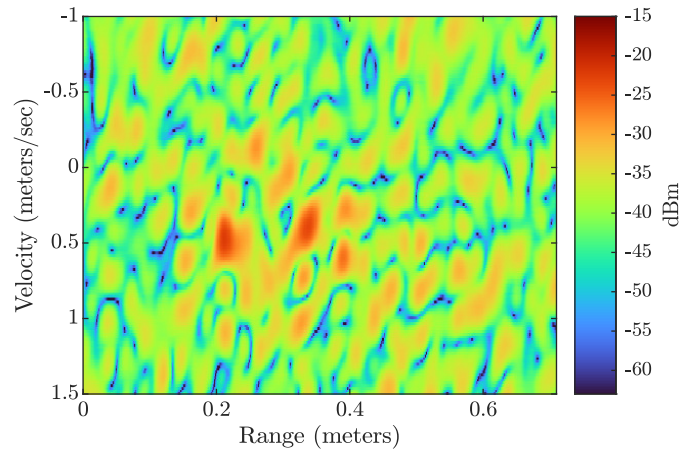


Fig. 5: Range-Doppler image for matched filter processing via (8) after background cancellation

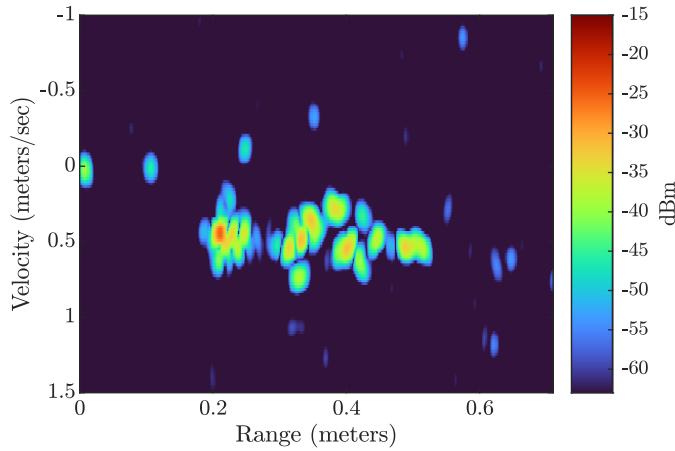


Fig. 6: Range-Doppler image after seven iterations of beamspoiled SPI via (16) with  $A=4$  and  $B=3$  after background cancellation (1st pulse)

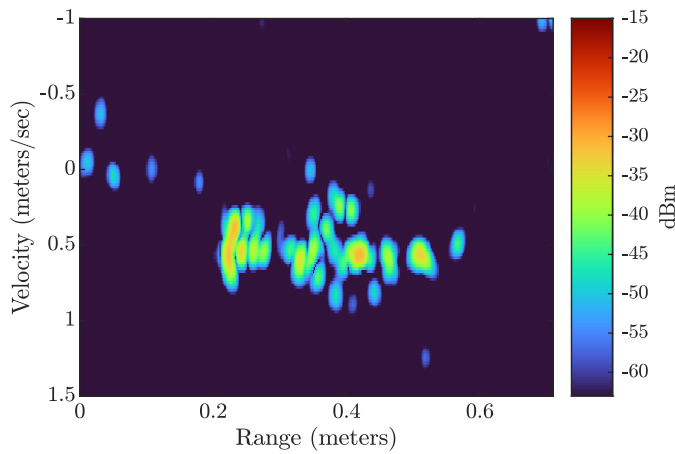


Fig. 7: Range-Doppler image after seven iterations of beamspoiled SPI via (16) with  $A=4$  and  $B=3$  after background cancellation (2nd pulse)

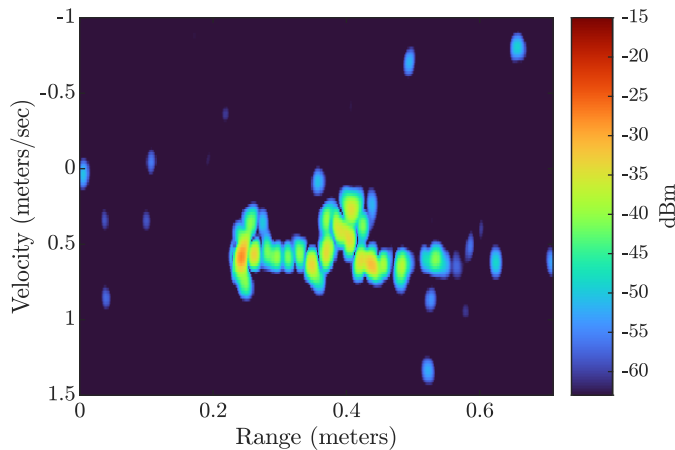


Fig. 8: Range-Doppler image after seven iterations of beamspoiled SPI via (16) with  $A=4$  and  $B=3$  after background cancellation (3rd pulse)

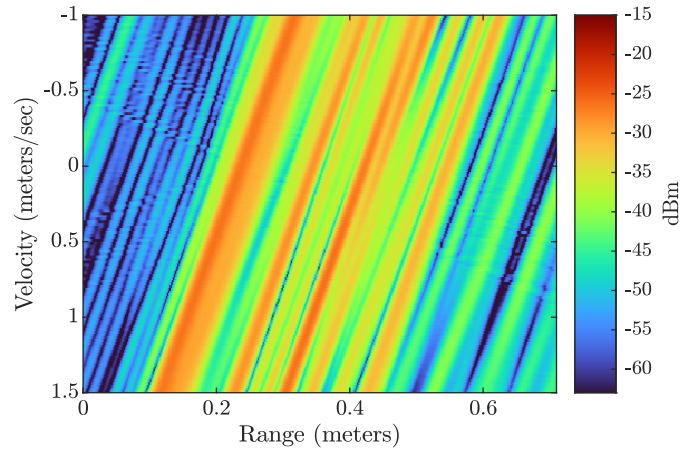


Fig. 9: Range-Doppler image for matched filter processing of LFM via (8) after background cancellation, illustrating the need for a Doppler-sensitive waveform

beamspoiled SPI are shown in Figs. 7 and 8. An oscillatory behavior in power and extent of the leading edge of the tricycle becomes visible, with a similar oscillating effect occurring about midway along the body. While it is difficult to say definitively, these aspects are presumed to be caused by rotation of the wheels and pedals, with the latter in particular rotating toward and away in alternating fashion as has been observed for micro-Doppler phenomenology [25–28]. The presentation that accompanies this paper includes a movie with data processed over several pulses to illustrate the evolution.

For the sake of completeness, Fig. 9 shows the matched filter response resulting from an LFM waveform. The Doppler tolerance of LFM is clearly indicated by the diagonal smearing, ultimately making visibility impossible. In short, a Doppler sensitive waveform is necessary in this context.

## VII. CONCLUSIONS

The RMMSE-based approach denoted as single pulse imaging (SPI) has been experimentally demonstrated using ultrasonic measurements collected at the University of Kansas, emulating the expected behavior at RF. This manner of adaptive processing enhances signal separation in both delay and fast-time Doppler for highly dynamic environments where stationarity cannot be assumed and sidelobes can mask the actual scattering structure. To provide necessary robustness, a model mismatch component and a new form of beamspoiling were each incorporated into SPI, collectively mitigating adverse super-resolution effects that would otherwise produce non-physical point-scattering results.

## REFERENCES

- [1] M.A. Richards, *Fundamentals of Radar Signal Processing*. McGraw-Hill, 2005.
- [2] N. Levanon and E. Mozeson, *Radar Signals*. Wiley – IEEE Press, 2004.
- [3] S.D. Blunt, and K. Gerlach, “Adaptive pulse compression via MMSE estimation,” *IEEE Transactions on Aerospace*

- and *Electronic Systems*, vol. 42, no. 2, pp. 572–584, Apr. 2006.
- [4] D. Henke, P. McCormick, S.D. Blunt, T. Higgins, “Practical aspects of optimal mismatch filtering and adaptive pulse compression for FM waveforms,” *IEEE Intl. Radar Conf.*, Washington, DC, May 2015.
- [5] S.D. Blunt, T. Chan, K. Gerlach, “Robust DOA estimation: The reiterative superresolution (RISR) algorithm,” *IEEE Transactions on Aerospace and Electronic Systems*, vol. 47, no. 1, pp. 332–346, Jan. 2011.
- [6] C.C. Jones, Z.E. Gannon, D. DePardo, J.W. Owen, S.D. Blunt, C.T. Allen, B.H. Kirk, “Development and experimental assessment of robust direction finding and self-calibration,” *IEEE Radar Conference*, New York City, NY, Mar. 2022.
- [7] M. Popescu, S.D. Blunt, T. Chan, “Magnetoencephalography source localization using the source affine image reconstruction (SAFFIRE) algorithm,” *IEEE Transactions on Biomedical Engineering*, vol. 57, no. 7, pp. 1652–1662, July 2010.
- [8] T. Cuprak, “Application of the reiterative MMSE algorithm to underwater acoustics using covariance matrix tapers for robustness,” Master’s thesis, George Mason University, 2013.
- [9] E. Yoshikawa, T. Ushio, Z. Kawasaki, S. Yoshida, T. Morimoto, F. Mizutani, M. Wada, “MMSE beam forming on fast-scanning phased array weather radar,” *IEEE Transactions on Geoscience and Remote Sensing*, vol. 51, no. 5, pp. 3077–3088, May 2013.
- [10] E. Méndez Domínguez, C. Magnard, M. Frioud, D. Small, E. Meier, “Adaptive pulse compression for range focusing in SAR imagery,” *IEEE Transactions on Geoscience and Remote Sensing*, vol. 55, no. 4, pp. 2262–2275, Apr. 2017.
- [11] C.C. Jones, L.A. Harnett, C.A. Mohr, S.D. Blunt, C.T. Allen, “Structure-based adaptive radar processing for joint clutter cancellation and moving target estimation,” *IEEE International Radar Conference*, Washington, DC, Apr. 2020.
- [12] L.A. Harnett, B. Ravenscroft, S.D. Blunt, C.T. Allen, “Experimental evaluation of adaptive doppler estimation for PRI-staggered radar,” *IEEE Radar Conference*, New York City, NY, Mar. 2022.
- [13] C.C. Jones, Z.E. Gannon, S.D. Blunt, C.T. Allen, A.F. Martone, “An adaptive spectrogram estimator to enhance signal characterization,” *IEEE Radar Conference*, New York City, NY, Mar. 2022.
- [14] S.D. Blunt, A.K. Shackelford, K. Gerlach, “Single pulse imaging,” *International Waveform Diversity and Design Conference*, Lihue, HI, Jan. 2006.
- [15] S.D. Blunt, A.K. Shackelford, K. Gerlach, K.J. Smith, “Doppler compensation and single pulse imaging using adaptive pulse compression,” *IEEE Transactions on Aerospace and Electronic Systems*, vol. 45, no. 2, pp. 647–659, Apr. 2009.
- [16] S.D. Blunt and K. Gerlach, “Multistatic adaptive pulse compression,” *IEEE Transactions on Aerospace and Electronic Systems*, vol. 42, no. 3, pp. 891–903, July 2006.
- [17] T. Yardibi, J. Li, P. Stoica, M. Xue, A.B. Baggeroer, “Source localization and sensing: A nonparametric iterative adaptive approach based on weighted least squares,” *IEEE Transactions on Aerospace and Electronic Systems*, vol. 46, no. 1, pp. 425–443, Jan. 2010.
- [18] B. Chen, Y. Dong, Y. Huang, J. Guan, X. Chen, “SRAP for range-coupled radar imaging,” *IET Radar, Sonar & Navigation*, vol. 14, no. 4, pp. 601–606, Feb. 2020.
- [19] P.M. McCormick, S.D. Blunt, T. Higgins, “A gradient descent implementation of adaptive pulse compression,” *IEEE Radar Conference*, Philadelphia, PA, May 2016.
- [20] M.A. Richards, J.A. Scheer, J. Scheer, W.A. Holm, *Principles of Modern Radar: Basic Principles, Volume I*. Electromagnetics and Radar, Institution of Engineering and Technology, 2010.
- [21] T. Higgins, S.D. Blunt, K. Gerlach, “Gain-constrained adaptive pulse compression via an MVDR framework,” *IEEE Radar Conference*, Pasadena, CA, May 2009.
- [22] S. Haykin, *Adaptive Filter Theory*. Prentice-Hall, 2002.
- [23] L. Harnett, *Mismatched Processing for Radar Interference Cancellation*. PhD thesis, University of Kansas, 2022.
- [24] J. Jakabosky, S.D. Blunt, B. Himed, “Spectral-shape optimized FM noise radar for pulse agility,” *IEEE Radar Conference*, Philadelphia, PA, May 2016.
- [25] D. Belgiovane and C.-C. Chen, “Micro-doppler characteristics of pedestrians and bicycles for automotive radar sensors at 77 GHz,” *European Conference on Antennas and Propagation*, Paris, France, Mar. 2017.
- [26] P. Held, D. Steinhauser, A. Kamann, A. Koch, T. Brandmeier, U.T. Schwarz, “Micro-doppler extraction of bicycle pedaling movements using automotive radar,” *IEEE Intelligent Vehicles Symposium (IV)*, pp. 744–749, Paris, France, June 2019.
- [27] R. Du, Y. Fan, J. Wang, “Pedestrian and bicyclist identification through micro doppler signature with different approaching aspect angles,” *IEEE Sensors Journal*, vol. 18, no. 9, pp. 3827–3835, Mar. 2018.
- [28] B. Rodriguez-Hervas, M. Maile, B.C. Flores, “Study of the microdoppler signature of a bicyclist for different directions of approach,” *SPIE*, May 2015.